RSC Advances

PAPER

View Article Online
View Journal | View Issue

Open Access Article. Published on 12 January 2026. Downloaded on 4/29/2026 2:22:39 PM.
This article is licensed under a Creative Commons Attribution-NonCommercial 3.0 Unported Licence.

Check for updates

Cite this: *RSC Adv.*, 2026, **16**, 2462

Green preparation of shell-based biochar and its adsorption of multi-component chlorinated volatile organic compounds

Dan He,[a] Jiao Wang,[a] Wei Deng,[a] Jiangbo Xiong,[b] Meijuan Lu,[b] Xiang Tu*[a] and Chenglong Yu *[b]

Received 18th September 2025
Accepted 21st December 2025

DOI: 10.1039/d5ra07060k

rsc.li/rsc-advances

This study applies a green method combining sodium phytate and sodium hydroxide to prepare hierarchical porous biochar from shell-based biomass waste (*e.g.*, pomelo peel, mandarin orange peel, orange peel, rice husk, and peanut shell). The resulting biochars have specific surface areas exceeding 2300 m^2 g^{-1}, with saturated adsorption capacities for chlorobenzene greater than 530 mg g^{-1}. The pomelo peel-derived biochar exhibited an exceptionally high chlorobenzene adsorption capacity of 572.5 mg g^{-1}. This outstanding performance is related to its high specific surface area (2331.19 m^2 g^{-1}), large micropore-specific surface area (1038.13 m^2 g^{-1}) and micropore volume (0.51 cm^3 g^{-1}), appropriate micro–mesoporous hierarchical structure (micropores accounting for 36.43%), abundant surface oxygen-containing functional groups, and disordered-graphitized microcrystalline structure. Volatile organic compound (VOC) adsorption experiments show that chlorobenzene adsorption has a distinct competitive advantage over benzene and toluene. This is attributed to its lower saturated vapor pressure, stronger polar interactions, smaller molecular kinetic diameter, and greater affinity and better matching with the available adsorption sites on the pomelo peel-derived biochar. By implementing green modification strategies, this work demonstrates high-value utilization of agricultural waste. The prepared hierarchical porous biochar exhibits excellent performance and significant application potential in the remediation of chlorinated VOCs, thus providing a novel pathway for the development of highly efficient VOC adsorption materials.

1 Introduction

Volatile organic compounds (VOCs) are a class of harmful pollutants that are ubiquitous in the atmospheric environment and are mainly derived from industrial production, daily life, and transportation emissions.[1] VOCs pose direct risks to human health and generate ozone (O_3) and fine particulate matter ($PM_{2.5}$) through photochemical reactions, thereby exacerbating the complex issue of atmospheric pollution.[2,3] In particular, chlorinated VOCs (*e.g.*, chlorobenzene and dichlorobenzene) are classified as priority pollutants owing to their high toxicity, persistence, and potential for bioaccumulation.[4] Adsorption is an effective strategy for treating and recovering chlorinated VOC emissions. Adsorption technology relies on the properties of the adsorbent, and the removal efficiency depends on the performance of the adsorbent.[5–7] In recent years, there has been growing interest in biochar-driven adsorption and removal of chlorinated VOCs.[8–10] Therefore, it is crucial to develop efficient and inexpensive VOC adsorption materials and treatment technologies to improve air quality and safeguard human health.

Biochar is a porous carbon-based material produced by the pyrolysis of biomass under oxygen-limited conditions. It has emerged as a research hotspot in the context of VOC adsorption due to its large specific surface area, abundant pore structure, diverse surface functional groups, and low cost.[11,12] The VOC adsorption performance of biochar is closely related to its pore structure (*i.e.*, proportions of micropores, mesopores, and macropores), surface chemical properties (*e.g.*, oxygen-containing functional groups, degree of graphitization), and the characteristics of the raw materials.[13–15] Raw biochar is often produced from agricultural and forestry waste, such as straw and sawdust, and its natural pore structure is predominantly microporous, resulting in limited VOC adsorption capacity. To overcome the performance limitations of conventional biochar, researchers often employ modification strategies to regulate its pore structure and surface chemical properties, thereby enhancing its adsorption capacity for specific pollutants.[16,17] Traditional chemical activation methods (*e.g.*, activation with

[a]*Jiangxi Provincial Key Laboratory of Environmental Pollution Control, Jiangxi Academy of Eco-Environmental Sciences and Planning, Nanchang 330039, China. E-mail: tuxiang527@163.com; Fax: +86-791-86866521; Tel: +86-791-86866521*

[b]*School of Land Resources and Environment, Jiangxi Agricultural University, Nanchang 330045, China. E-mail: chenglongyu888@163.com; Fax: +86-791-83813024; Tel: +86-791-83813024*

 © 2026 The Author(s). Published by the Royal Society of Chemistry

Open Access Article. Published on 12 January 2026. Downloaded on 4/29/2026 2:22:39 PM. This article is licensed under a Creative Commons Attribution-NonCommercial 3.0 Unported Licence.

KOH or $ZnCl_2$) can significantly increase the specific surface area of biochar. However, these approaches have notable drawbacks. For example, the pyrolysis process can generate reactive metals, such as potassium and zinc, which cause environmental pollution and corrode equipment.[18,19] Therefore, methods for the functional modification of biochar have attracted increasing attention, particularly the development of low-cost and green biochar modification techniques.

Shell-based biomass is generated by the agricultural and food processing industries and is characterized by enormous annual production and high susceptibility to decay. Direct disposal of such biomass leads to significant resource waste and environmental pollution. Shell-based biomass is rich in cellulose, hemicellulose, and lignin, and as a result, pyrolysis carbonization can produce a rich pore structure. However, its natural pore structure is predominantly microporous, and the biochar surface is relatively inert, enabling only limited VOC adsorption.[20] Studies have shown that appropriate modifications can optimize the biochar pore structure and increase the amount of surface oxygen-containing functional groups, thereby enhancing its VOC adsorption capacity.[21,22] The combined activation method (using sodium phytate and sodium hydroxide) achieves synergistic organic–inorganic effects, optimizing both the pore structure and surface chemical properties of the obtained biochar. The resulting properties are beneficial for the adsorption and removal of heavy metals, organic pollutants, and other contaminants.[23] A previous report proposed a Cd(II) adsorption mechanism for bamboo-derived biochar modified with sodium phytate.[24] However, there has been limited research focusing on the preparation of hierarchical porous biochar from shell-based biomass *via* combined sodium phytate and sodium hydroxide modification and its applications for chlorinated VOC adsorption.

Aiming to fill this knowledge gap, the present study used shell-based biomass agricultural waste as raw materials in a combined sodium phytate/sodium hydroxide modification method to prepare hierarchical porous biochar. Thorough characterization and systematic analysis revealed the effects of physicochemical properties (*e.g.*, pore structure, surface chemical properties, and thermal stability) on the adsorption performance of the hierarchical porous biochar. The structure–activity relationships were also investigated, and the competitive adsorption mechanism for multi-component chlorinated VOCs was explored.

2 Materials and methods

2.1 Experimental materials

The shell biomass (*i.e.*, peels) used in this study, including pomelo peel (PP), orange peel (OP), and mandarin orange peel (MP), were purchased from a nearby fruit shop; rice husk (RH) and peanut shell (PS) were obtained from a local farmers' market. The composition of the raw materials is a critical factor dictating the properties of the synthesized biochar materials. The elemental analysis results for the biomass feedstocks are presented in Table 1. Sodium phytate (99%) was purchased from Macklin Biochemical Technology Co., Ltd (Shanghai, China). Benzene (analytical grade), toluene (analytical grade), and chlorobenzene (analytical grade) were obtained from Sinopharm Chemical Reagent Co., Ltd (Shanghai, China). Sodium hydroxide (analytical grade) was purchased from Henan Hongchang Chemical Co., Ltd. High-purity nitrogen, oxygen, and argon gases were obtained from Nanchang Guoteng Gas Co., Ltd.

Table 1 Elemental analyses of biomass raw materials

Material	N (%)	C (%)	H (%)	O (%)	C/N	H/C	O/C
PP	1.08	41.71	6.68	40.58	1.03	0.16	0.97
MP	1.22	42.62	6.64	38.60	1.10	0.16	0.91
OP	0.96	41.88	6.63	40.08	1.04	0.16	0.96
RH	0.39	41.34	5.63	33.30	1.24	0.14	0.81
PS	0.89	45.63	5.92	34.44	1.32	0.13	0.75

2.2 Preparation of shell-based biochars

2.2.1 Gel pre-treatment. The biomass raw materials, including PP, MP, OP, RH, and PS, were dried at 105 °C to a constant weight and then ground and sieved to obtain particles smaller than 20 mesh. Pomelo peel powder was mixed with sodium phytate in a mass ratio of 1 : 2 in a beaker that was prefilled with 20 mL of deionized water. The beaker was then placed in a constant-temperature water bath at 60 °C and stirred to induce a sol–gel reaction. The viscosity of the solution gradually increased as the reaction proceeded over 5 hours, eventually turning reddish-brown. The resulting mixture was removed and placed in an oven at 105 °C for drying and curing, ultimately yielding a solid gel.

2.2.2 High-temperature pyrolysis. The gel was ground and then calcined in a tube furnace under a nitrogen atmosphere at a rate of 10 °C min^{-1} up to 450 °C where it was held for 2 hours. After cooling to room temperature, the sample was removed and further pyrolyzed with sodium hydroxide in a mass ratio of 1 : 2 under a nitrogen atmosphere at a rate of 5 °C min^{-1} up to 700 °C where it was held for 2 hours. After cooling again to room temperature, the product was removed and washed with 0.5 mol L^{-1} hydrochloric acid and deionized water *via* vacuum filtration until the pH of the washing solution reached neutrality. The material was then dried at 105 °C and stored in sealed bags for subsequent use. All shell-based biochars were prepared using the same method (Fig. 1).

2.3 Characterization of shell-based biochars

The physicochemical properties of the prepared biochars were characterized using nitrogen adsorption/desorption (Brunauer–Emmett–Teller; BET) analysis, scanning electron microscopy (SEM), Fourier transform infrared spectroscopy (FTIR), Raman spectroscopy, X-ray photoelectron spectroscopy (XPS), elemental analysis, and thermogravimetric analysis (TGA). The instrumental details and testing parameters are detailed in the SI.

2.4 Adsorption of multi-component VOCs onto shell-based biochars

Gas-phase adsorption experiments were conducted in a laboratory-built fixed-bed reactor. The evaluation setup comprised

Open Access Article. Published on 12 January 2026. Downloaded on 4/29/2026 2:22:39 PM.
This article is licensed under a Creative Commons Attribution-NonCommercial 3.0 Unported Licence.

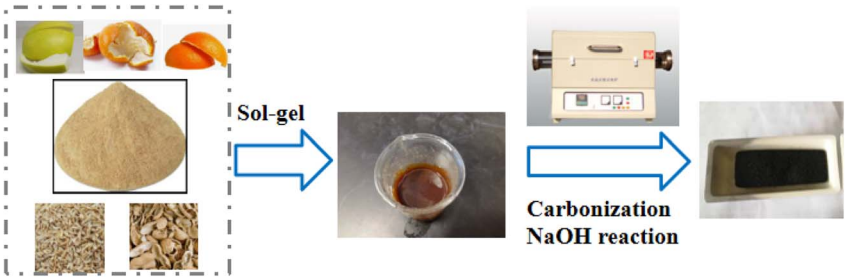

Fig. 1 Flow diagram of shell-derived biochar preparation.

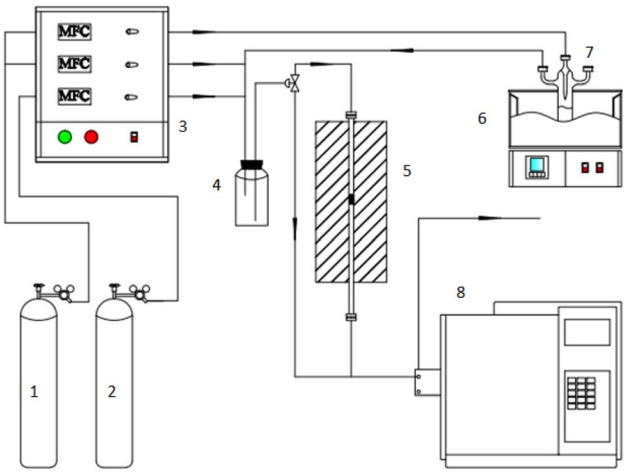

Fig. 2 Dynamic adsorption experimental apparatus (1 = nitrogen, 2 = dry air, 3 = flow controller, 4 = buffer flask, 5 = adsorber, 6 = incubator, 7 = bubbling flask, 8 = gas chromatograph).

a gas supply system, a biochar adsorption system, and a gas chromatography (GC) analytical system (Fig. 2). To simulate realistic adsorption conditions, the experiments were performed under atmospheric pressure, rather than under vacuum. Benzene, toluene, and chlorobenzene were introduced into the system by bubbling the carrier gas (N_2) through the respective liquid reagents. The initial concentrations of these VOCs were each controlled at approximately 300 mg m^{-3}, with a flow rate of 100 mL min^{-1}. The temperature of the adsorption column was maintained at 40 °C, and the biochar loading was 50 mg. The concentrations of benzene, toluene, and chlorobenzene in the outlet gas were analyzed using a gas chromatograph (FULI 9790, CN) equipped with a flame ionization detector (FID). The adsorption capacities were calculated by plotting the variations in the outlet concentrations of the VOCs over time and integrating the curves. The formula for calculating the adsorption capacity is provided in the SI.

3 Results and discussion

3.1 Single-component VOC adsorption by shell-based biochars

The adsorption performances of shell-based biochars were systematically evaluated based on dynamic adsorption experiments conducted using a self-assembled fixed-bed reactor at 40 °C. Five shell-derived biochars were tested in terms of their chlorobenzene adsorption, and their adsorption characteristics were quantified by plotting dynamic adsorption breakthrough curves (Fig. 3). The breakthrough curves of all materials exhibited typical S-shaped three-stage patterns. In the initial stage, the active sites on the adsorbent surface were rapidly occupied by chlorobenzene molecules, resulting in a linear increase in adsorption capacity over time. In the intermediate stage, as the micropores gradually became filled, the adsorption rate slowed due to the diffusion resistance of chlorobenzene molecules within the mesopores. As a result, the slope of the curve decreased. In the saturation stage, with the micropores nearing full capacity, chlorobenzene molecules began to break through the adsorbent layer. Thus, the outlet concentration gradually approached the inlet concentration, eventually reaching adsorption saturation.

The different materials' breakthrough adsorption capacities and saturation adsorption capacities for chlorobenzene were obtained by integrating the breakthrough curves (Fig. 4 and Table 2). Although the overall trends observed in the breakthrough curves for the five materials were similar, their adsorption performances varied significantly. For example, PP biochar and MP biochar exhibited comparable saturation times (approximately 440 minutes); however, PP biochar had a higher saturation adsorption capacity for chlorobenzene (572.5 mg

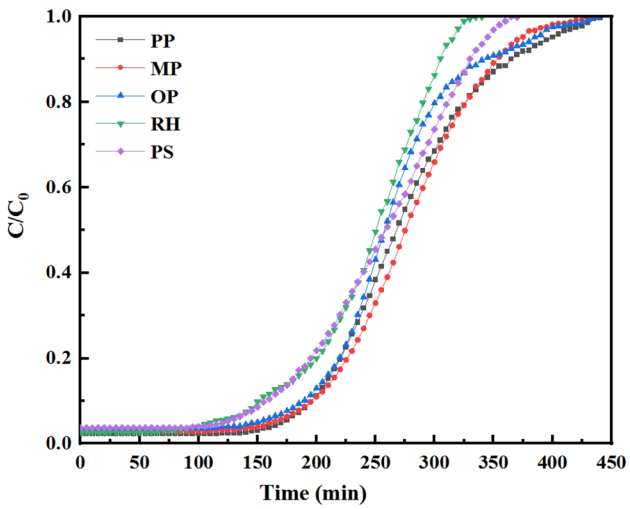

Fig. 3 Dynamic chlorobenzene adsorption curves for shell-derived biochars.

 © 2026 The Author(s). Published by the Royal Society of Chemistry

Open Access Article. Published on 12 January 2026. Downloaded on 4/29/2026 2:22:39 PM.
This article is licensed under a Creative Commons Attribution-NonCommercial 3.0 Unported Licence.

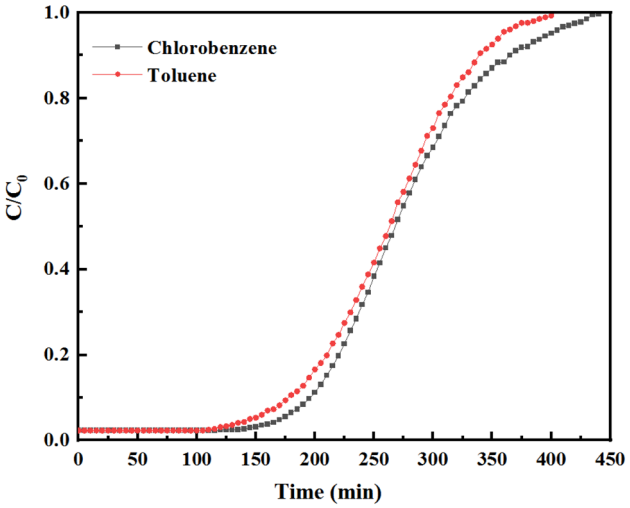

Fig. 4 PP biochar dynamic adsorption penetration curves for toluene/chlorobenzene.

g^{-1}). Overall, the breakthrough times and breakthrough adsorption capacities of the five biochar materials for chlorobenzene differed significantly, but they followed similar trends, *i.e.*, the performance decreased in the order, PP > MP > OP > PS > RH.

To compare the adsorption performances of shell-based biochars for different single-component VOCs, the adsorption of toluene and chlorobenzene by PP biochar were evaluated individually. The dynamic toluene and chlorobenzene adsorption breakthrough curves of PP biochar were plotted (Fig. 4), and the corresponding breakthrough adsorption capacities and saturation adsorption capacities were calculated (Table 3). The saturation adsorption capacity and breakthrough adsorption capacity of PP biochar for chlorobenzene were both higher than those for toluene (572.5 mg g^{-1} *vs.* 560.6 mg g^{-1} and 360.9 mg g^{-1} *vs.* 317.9 mg g^{-1}, respectively). Therefore, the adsorption performance of PP biochar for chlorobenzene was superior to that for toluene.

3.2 Physicochemical properties of shell-based biochars

3.2.1 Pore characteristics. Nitrogen adsorption–desorption experiments were conducted to systematically investigate the pore structure characteristics of shell-based biochar materials, and the nitrogen adsorption–desorption isotherms are shown in Fig. 5. The isotherms of all shell-based biochars exhibited composite Type I and Type IV patterns, suggesting that the materials comprised hierarchical pore structures dominated by micropores, along with the development of mesopores. In the low relative pressure range ($P/P_0 < 0.1$), the nitrogen adsorption capacity increased rapidly, indicating the presence of numerous micropores or micropore-like defect sites on the material surface. This behavior is characteristic of a Type I isotherm, and this region contributes significantly to micropore adsorption. As the relative pressure increased ($P/P_0 > 0.1$), the rate of adsorption growth slowed and gradually approached saturation. Notably, when $P/P_0 > 0.5$, a distinct H4-type hysteresis loop was observed. This is typically associated with slit-like mesoporous structures, further confirming that the samples contained mesopores in addition to micropores. Therefore, the overall pore structure of the materials could be characterized as hierarchical pore systems with coexisting micropores and mesopores.[25] Sodium phytate is a green chelating agent that complexes with metal ions (*e.g.*, Ca^{2+}, Mg^{2+}) in biomass at low temperatures. Upon high-temperature pyrolysis, it forms an inorganic salt framework that stabilizes the carbon skeleton at elevated temperatures, thus preventing the collapse of the pore structure. Sodium hydroxide is a common activating agent that further promotes pore development by removing soluble components, such as sugars and lignin, from the biomass. The phosphate groups in sodium phytate may also react with sodium hydroxide, thereby intensifying the activation reaction. The combined use of sodium phytate and sodium hydroxide produces a synergistic pore-forming effect that supports the construction of a well-developed micro–mesoporous hierarchical structure. This approach regulates the ratio of micropores to mesopores more effectively than using either reagent alone.[26,27]

The pore structure parameters of each shell-based biochar sample were further extracted and analyzed based on the nitrogen adsorption data (Table 4). After the combined modification treatment with sodium phytate and sodium hydroxide, the specific surface areas (SSA) of all shell-based biochar samples were significantly enhanced, each exceeding 2300 m^2 g^{-1}, with the highest reaching 2466.40 m^2 g^{-1}. Notably, the type of raw material had a relatively minor impact on the total SSA of the modified biochars, but it had a significant influence on the development of the microporous structure. In other words, the micropore-related structural parameters, including micropore SSA, micropore volume, and the proportion of micropore volume relative to the total pore volume, showed notable variations among the different shell-based biochars. In particular, PP biochar exhibited the most highly developed microporous structure, with a micropore SSA of 1038.13 m^2 g^{-1}, a micropore volume of 0.51 cm^3 g^{-1}, and a micropore volume fraction of up

Table 2 Chlorobenzene adsorption capacities of shell-derived biochars

Adsorbent	Breakthrough time (min)	Breakthrough adsorption capacity (mg g^{-1})	Saturation time (min)	Saturation adsorption capacity (mg g^{-1})
PP	175	360.9	440	572.5
MP	170	343.5	440	565.5
OP	155	326.9	430	562.8
RH	115	256.5	340	531.5
PS	125	270.5	365	557.6

Open Access Article. Published on 12 January 2026. Downloaded on 4/29/2026 2:22:39 PM.
This article is licensed under a Creative Commons Attribution-NonCommercial 3.0 Unported Licence.

Table 3 Toluene and chlorobenzene adsorption capacities of PP biochar

Adsorbate	Breakthrough time (min)	Breakthrough adsorption capacity (mg g^{-1})	Saturation time (min)	Saturation adsorption capacity (mg g^{-1})
Chlorobenzene	175	360.9	440	572.5
Toluene	150	317.9	430	560.6

to 36.43% of the total pore volume, which was the highest among all tested samples. These results were attributed to the following factors. First, the relatively high lignin content in pomelo peel facilitates the formation of a highly cross-linked and structurally stable aromatic carbon skeleton during pyrolysis, which serves as the fundamental framework for micropore development. Additionally, although pomelo peel (along with tangerine and orange peels) belongs to the citrus family and represents a similar biomass category, pomelo peel is distinguished by its exceptionally thick spongy layer and inherently loose macroporous structure. This results in a more developed initial pore network than with other citrus peels, likely providing a larger surface area for the penetration and reaction of activating agents and promoting the formation of uniform pores. Furthermore, specific inorganic components in pomelo peel, such as potassium salts, can act as self-activating agents during pyrolysis, thereby inducing a synergistic effect with sodium phytate and sodium hydroxide.[28] In general, the micropore SSA, micropore volume, and micropore proportion all decreased in the order, PP > MP > OP > PS > RH. These trends in micropore structural parameters were consistent with those observed for the biochars in terms of chlorobenzene breakthrough adsorption capacity and breakthrough time. These findings indicate that the microporous structure of shell-based biochar is a key factor influencing its chlorobenzene adsorption performance.

In terms of the adsorption mechanism, VOC adsorption by a biochar material relies primarily on its pore structure, particularly the microporous structure, which is the key contributor of adsorption sites. The high SSA and small dimensions of micropores enable effective physical adsorption of chlorobenzene molecules.[29] Mesopores contribute to enhanced adsorption capacity under higher vapor pressure conditions through the capillary condensation effect, whereas

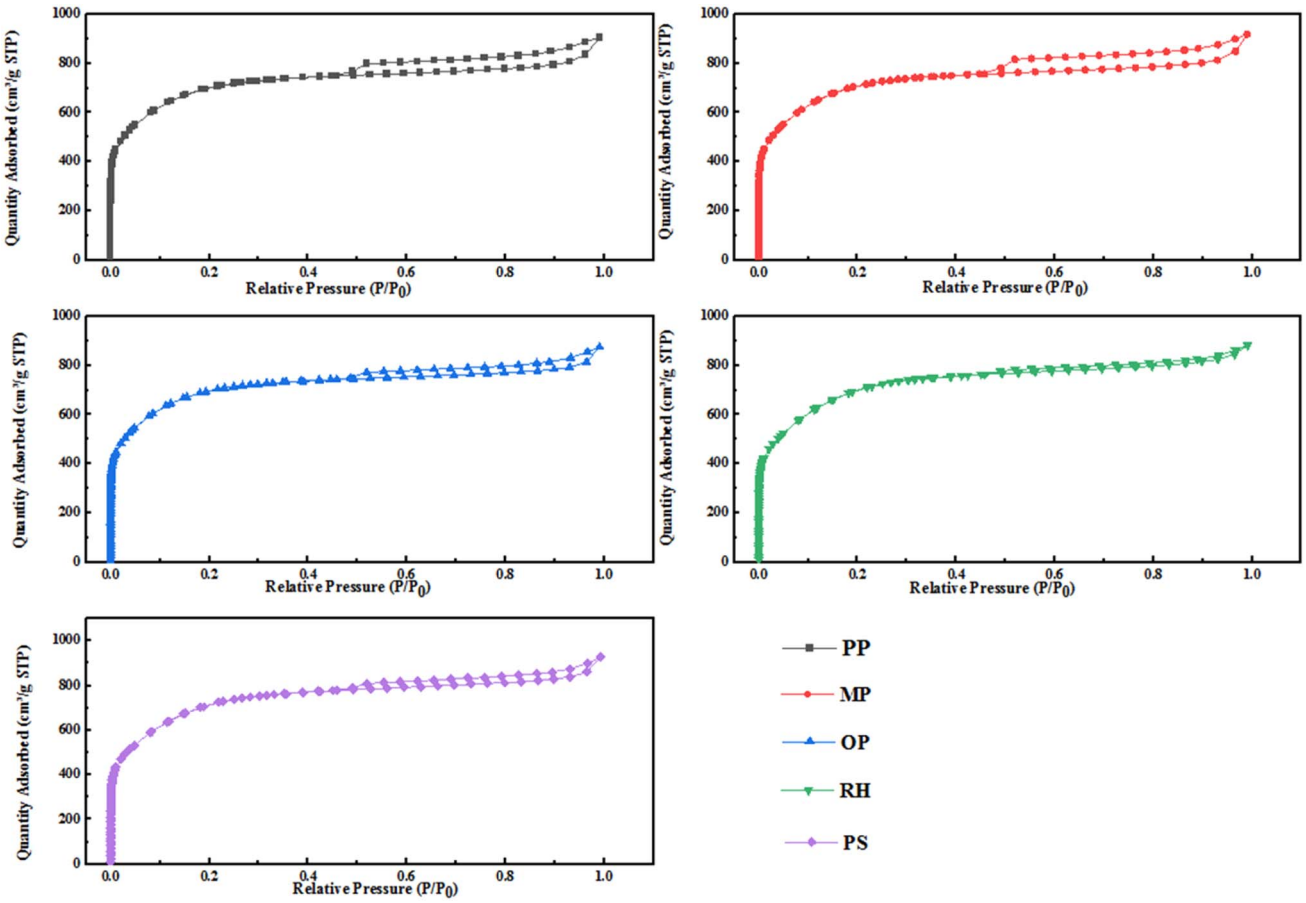

Fig. 5 Shell-derived biochars' nitrogen adsorption and desorption isotherms.

 © 2026 The Author(s). Published by the Royal Society of Chemistry

Open Access Article. Published on 12 January 2026. Downloaded on 4/29/2026 2:22:39 PM.
This article is licensed under a Creative Commons Attribution-NonCommercial 3.0 Unported Licence.

Table 4 Pore structure parameters of shell-derived biochars

Adsorbent	S_{BET} (m^2 g^{-1})	S_{mic} (m^2 g^{-1})	V_{total} (cm^3 g^{-1})	V_{mic} (cm^3 g^{-1})	V_{mes} (cm^3 g^{-1})	V_{mic}/V_{total} (%)
PP	2331.19	1038.13	1.4	0.51	0.89	36.43
MP	2352.42	1021.9	1.42	0.5	0.92	35.21
OP	2300.74	903.66	1.36	0.46	0.9	33.82
RH	2420.33	583.51	1.37	0.27	1.1	19.71
PS	2466.40	618.01	1.44	0.29	1.16	20.14

macropores mainly serve as mass transfer pathways. Although macropores make a limited contribution to adsorption capacity, they facilitate the diffusion and transport of gas molecules within the biochar matrix.[30,31] In this study, the PP biochar sample had the highest SSA and the most highly developed microporous structure, which endowed it with optimal adsorption performance in the chlorobenzene adsorption experiments. In contrast, although the PS biochar sample had the highest total SSA (2466.40 m^2 g^{-1}), its microporous structure was relatively underdeveloped ($S_{mic} = 618.01$ m^2 g^{-1}, $V_{mic} = 0.29$ cm^3 g^{-1}, $V_{mic}/V_{total} = 20.14\%$), resulting in a weaker adsorption performance. In summary, the well-developed microporous structure within shell-based biochars, along with the hierarchical pore structure generated through the synergistic contribution of mesopores, provide a key structural basis for efficient chlorobenzene adsorption. Among the tested materials, PP biochar demonstrated the best chlorobenzene adsorption performance, consistent with its favorable pore structure characteristics (*i.e.*, large SSA, the most developed microporous structure, and an optimized micro–mesopore ratio).[32]

3.2.2 Surface morphologies. The surface morphologies of the shell-based biochars were observed using SEM (Fig. 6). The surfaces of the biochars prepared from all five types of raw materials exhibited rough and uneven features, with pore structures of varying sizes distributed across the surface. Because the amount of sodium phytate added during the modification was kept consistent, there were minimal

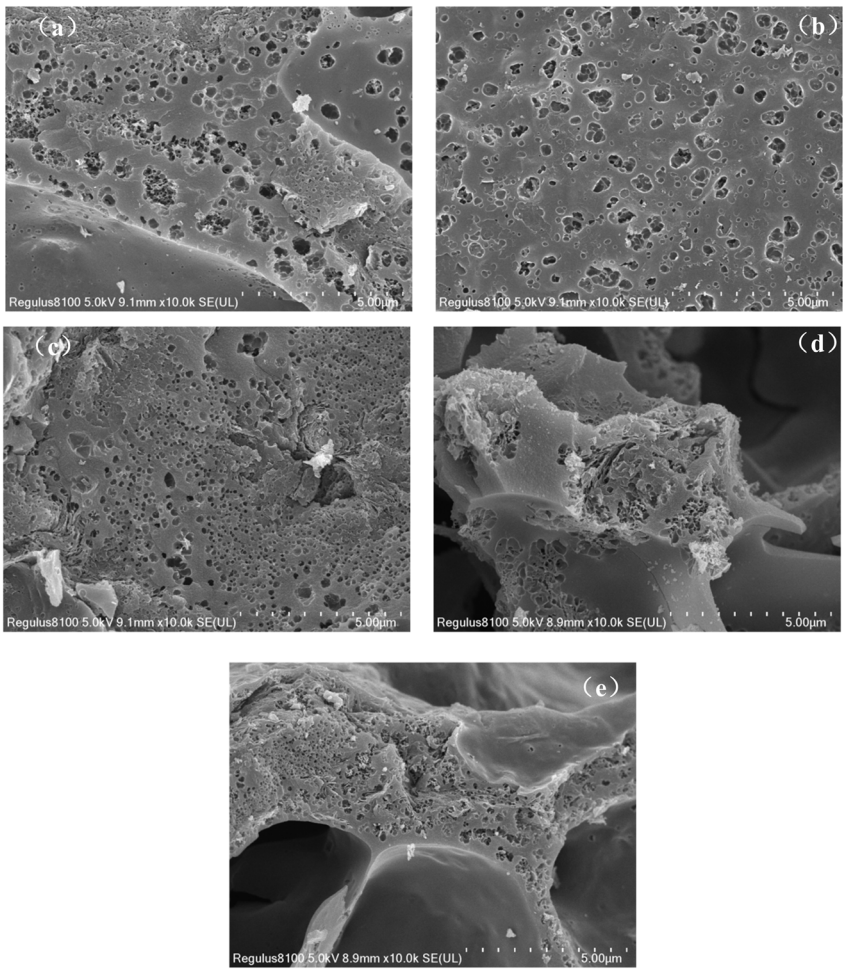

Fig. 6 SEM images of biochars derived from (a) PP, (b) MP, (c) OP, (d) RH, and (e) PS.

Open Access Article. Published on 12 January 2026. Downloaded on 4/29/2026 2:22:39 PM.
This article is licensed under a Creative Commons Attribution-NonCommercial 3.0 Unported Licence.

differences in the surface morphologies of the biochars derived from different raw materials. The biochars prepared in this study had clearly identifiable pore structures, with numerous micro-defects on the pore surfaces, indicating that the mesopore walls were covered with abundant micropores. This is characteristic of typical amorphous porous carbon materials. These surface morphologies were also consistent with the hierarchical porous structures revealed by nitrogen adsorption–desorption isotherms, and with key BET parameters, such as SSA and pore volume. Moreover, these features were related to the strong chlorobenzene adsorption performances of the biochars.

The chelating agent, sodium phytate, exhibited stepwise weight loss during pyrolysis. The weight loss between room temperature and 200 °C was primarily due to the removal of crystalline water. When the temperature exceeded 280 °C, polycondensation between sodium phytate molecules released small gaseous molecules and formed sodium pyrophosphate ($Na_4P_2O_7$). As the temperature increased to 450 °C, the weight of sodium phytate stabilized. Notably, at 650 °C, sodium phytate underwent a solid-state reaction with sodium hydroxide, producing stable inorganic salt particles, such as sodium carbonate (Na_2CO_3) and sodium phosphate (Na_3PO_4). Owing to the high thermal stability of these inorganic salts, neither decomposed or reacted with the carbon skeleton. Instead, they acted as template agents that became embedded within the shell-based biochars. Some of these particles aggregated to form larger templates, which were eventually removed when washing with deionized water and hydrochloric acid, leaving behind a rich pore structure within the carbon material.[26]

The activating agent, sodium hydroxide, created numerous defects on the pore walls through its etching effect, thereby promoting the development of the microporous structure. However, activation with sodium hydroxide alone typically results in predominantly microporous biochars.[33] In this study, the shell-based biomass first underwent a sol–gel reaction with sodium phytate to form a pre-structured material, which was then carbonized. Subsequently, a solid-state reaction with sodium hydroxide was carried out *in situ* to generate nano-scale templates. This process, combined with the activating and etching effects of sodium hydroxide, led to the formation of a hierarchical porous carbon material with a well-developed micro–mesoporous structure. This hierarchical pore structure provides ample mass transfer space and abundant active sites for the adsorption of VOCs, providing the structural basis for the materials' excellent adsorption performances.

3.2.3 Surface functional groups. FTIR spectroscopy was used to systematically investigate the differences in surface functional groups on the biochars derived from various shell-based biomass materials after modification with sodium phytate and sodium hydroxide (Fig. 7). All sample spectra had characteristic peaks at 3420, 2923, and 1630 cm^{-1}. The broad peak at 3420 cm^{-1} was attributed to the O–H stretching vibration (*e.g.*, of alcohols, phenols, and aldehydes). The peak at 2923 cm^{-1} corresponded to the C–H stretching vibration originating from aliphatic groups, such as $-CH_3$. The peak at 1630 cm^{-1} was related to the stretching vibrations of C=O

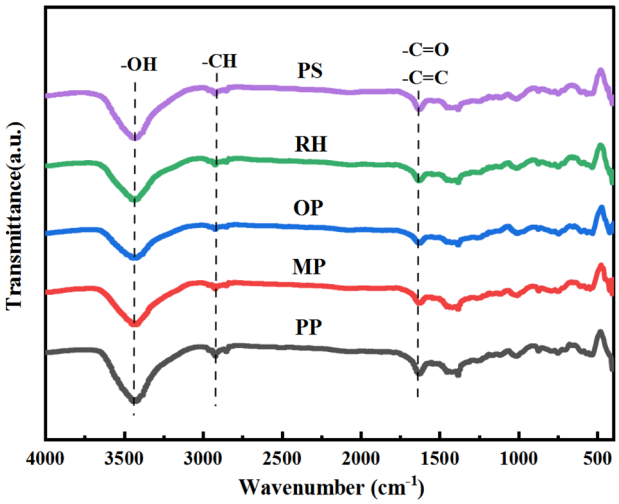

Fig. 7 Shell-derived biochar FTIR spectra.

(carbonyl) or C=C (carboxyl or conjugated carbonyl groups).[17] These characteristic peaks indicated that the surfaces of the shell-based biochar materials were rich in oxygen-containing functional groups, including hydroxyl (–OH), carboxyl (–COOH), and carbonyl (C=O) groups. These oxygen-containing functional groups can synergistically enhance the adsorption of chlorobenzene through π–π conjugation interactions and hydrogen bonding effects. Specifically, the lone pair electrons of the functional groups interact weakly with the π-electron cloud of the chlorobenzene aromatic ring (π–π interactions), thereby increasing molecular affinity. Meanwhile, the polar groups of chlorobenzene molecules (*e.g.*, C–Cl bonds) can form hydrogen bonds with oxygen-containing functional groups (*e.g.*, –OH), thereby increasing the binding stability between the adsorption sites and the target molecules. This multi-interaction mechanism between functional groups and the adsorbate (*i.e.*, chlorobenzene) provides a surface chemical basis for the efficient adsorption of chlorobenzene by shell-based biochars.

3.2.4 Degree of graphitization and defect density. Raman spectroscopy was used to characterize the degree of graphitization and defect density of the shell-based biochar materials (Fig. 8). All five biochar samples exhibited two distinct peaks. The D peak at 1360 cm^{-1} was attributed to the disordered carbon structure (*i.e.*, the disordered aromatic bands of condensed aromatic units) and is typically associated with irregular, disordered "turbostratic" carbon layers. The G peak at 1580 cm^{-1} was attributed to the in-plane vibrations of sp^2 carbon atoms in graphite microcrystals, indicating the presence of an ordered graphitic structure. These results suggest that all five of the prepared biochar materials contained a combination of disordered and graphitic carbon structures. However, the intensities of the D and G peaks differed among the samples, reflecting the variations in their defect levels and degrees of graphitization. The intensity ratio of the D peak to the G peak (I_D/I_G) can be used as a qualitative indicator of the graphitization and defect status of carbon materials. In this study, PP biochar had the lowest I_D/I_G ratio, suggesting that it contained the fewest defects and had the highest degree of graphitization.

 © 2026 The Author(s). Published by the Royal Society of Chemistry

Open Access Article. Published on 12 January 2026. Downloaded on 4/29/2026 2:22:39 PM.
This article is licensed under a Creative Commons Attribution-NonCommercial 3.0 Unported Licence.

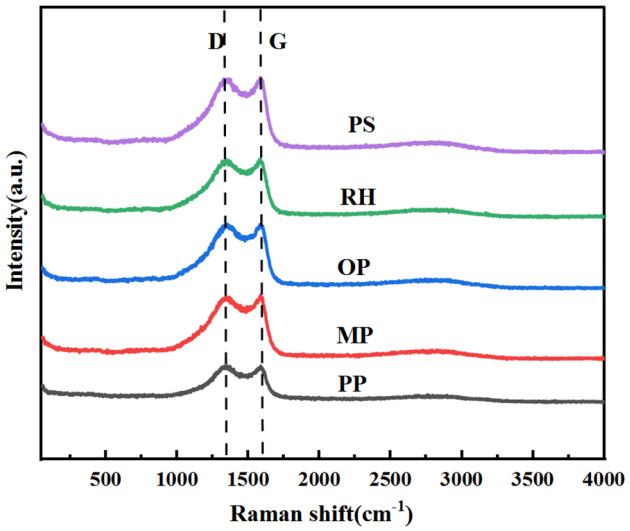

Fig. 8 Shell-derived biochar Raman spectra.

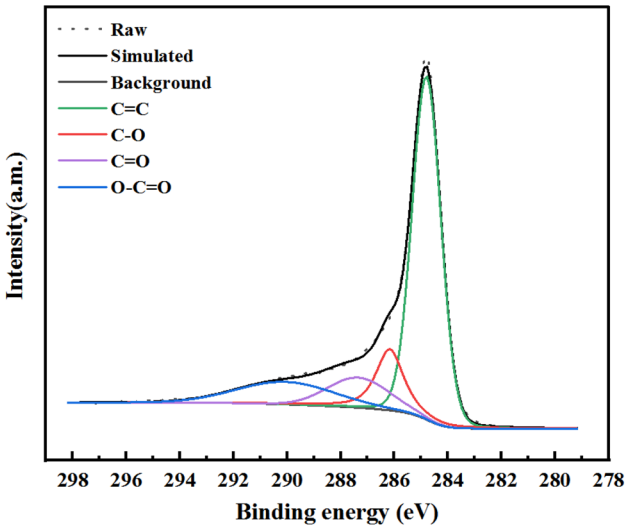

Fig. 9 PP biochar XPS spectrum and fitting.

This was likely related to the higher lignin content in pomelo peel, which facilitates the formation of short-range ordered structures during carbonization. This structural characteristic was also consistent with PP biochar's superior chlorobenzene adsorption capacity, highlighting the roles of graphitization and defect structure in determining adsorption performance.

3.2.5 Surface chemical compositions. High-resolution XPS analysis of the C1s orbital was conducted to further analyze the surface chemical composition of PP biochar and its interactions with chlorobenzene. The C1s XPS spectrum of PP biochar contained four distinct characteristic peaks. After fitting with reference binding energy data, these peaks at 284.8, 286.1, 287.3, and 289.2 eV were assigned to aromatic C=C bonds (aromatic carbon skeleton), C–O bonds (*e.g.*, in alcohols or ethers), C=O bonds (carbonyl groups), and O–C=O bonds (carboxyl groups, –COOH), respectively. These results indicated that the surface of PP biochar was rich in aromatic carbon frameworks and oxygen-containing functional groups, including C–O, C=O, and COOH. These surface chemical groups worked synergistically through multiple interaction mechanisms to enhance chlorobenzene adsorption. For example, the aromatic C=C bonds on the PP biochar surface formed π–π conjugation interactions with the benzene ring of chlorobenzene molecules. This interaction, driven by electron cloud overlap, significantly enhanced molecular affinity. The polar C–O (C–O–H/C–O–C) and C=O bonds acted as polar functional groups, which engaged in dipole–dipole interactions or formed hydrogen bonds with the polar C–Cl bond in chlorobenzene, thereby facilitating stable binding. The carboxyl group (–COOH) partially dissociated into $-COO^-$ ions in solution, providing strong electrostatic adsorption sites. These negatively-charged sites had electrostatic attraction with the chlorobenzene molecules, further stabilizing their adsorption on the biochar surface. Together, these surface chemical features and multifaceted interactions contributed to PP biochar's optimal chlorobenzene adsorption performance, consistent with the aforementioned adsorption evaluation results (Fig. 9).

3.2.6 Thermal stability. TGA was conducted with PP biochar under an air atmosphere to evaluate its thermal stability (Fig. 10). When the temperature was below 100 °C, the PP biochar underwent an approximate 10% mass loss, which was primarily attributed to the evaporation of moisture and other volatile impurities that the sample had adsorbed during storage. A more significant mass loss occurred in the temperature range of 400–500 °C due to the oxidative reaction between the biochar and oxygen in the air at high temperatures, leading to the formation of carbon dioxide (CO_2) and rapid mass reduction. Above 500 °C, the mass generally stabilized, reflecting the residual carbon skeleton of the biochar. Overall, there was no significant mass loss below 400 °C, indicating that the PP biochar maintains structural stability from ambient to medium temperatures (<400 °C) and has relatively good thermal stability. This property makes it suitable for VOC adsorption applications, for which the adsorption temperatures

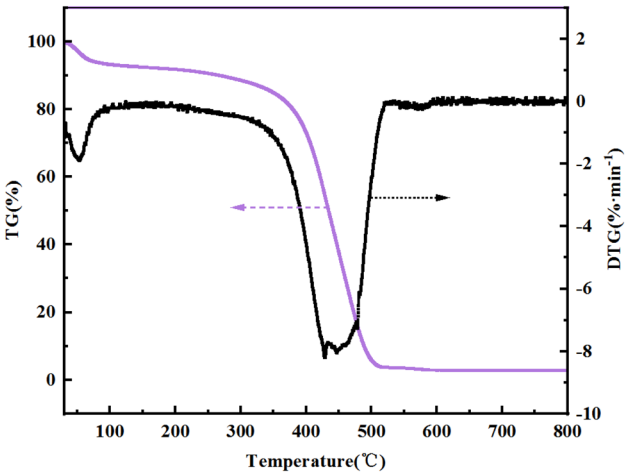

Fig. 10 TGA of PP biochar.

Open Access Article. Published on 12 January 2026. Downloaded on 4/29/2026 2:22:39 PM.
This article is licensed under a Creative Commons Attribution-NonCommercial 3.0 Unported Licence.

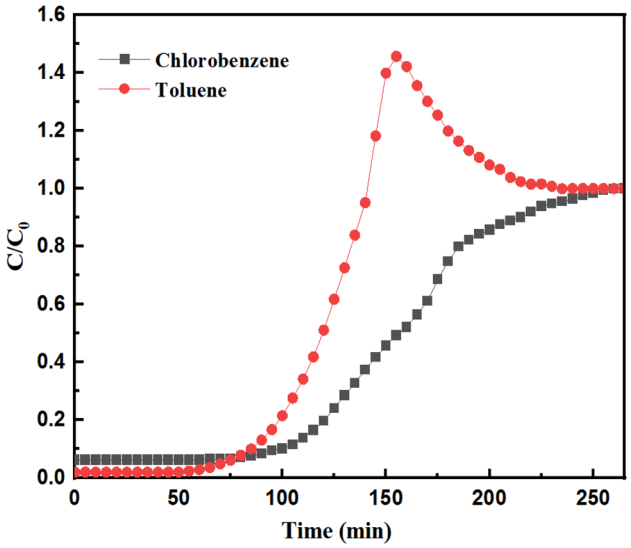

Fig. 11 Dynamic adsorption curves of toluene and chlorobenzene on PP biochar.

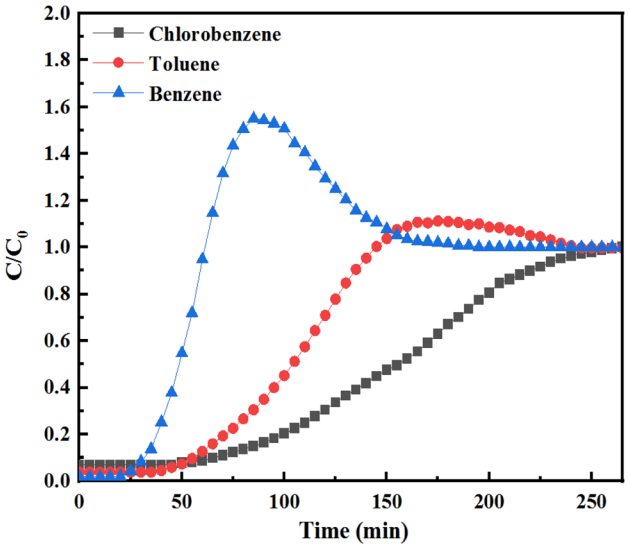

Fig. 12 Dynamic adsorption curves of benzene, toluene, and chlorobenzene on PP biochar.

are typically ≤150 °C (*e.g.*, chlorobenzene boiling point = 131 °C). The thermal stability of PP biochar prevents adsorption capacity degradation caused by thermal decomposition, thus demonstrating potential for industrial applications.

3.3 Competitive adsorption mechanism of shell-based biochars for multi-component VOCs

3.3.1 Multi-component VOC adsorption performances of shell-based biochars. In practical industrial production, VOCs are often emitted as multi-component mixtures.[34,35] Therefore, it is critical to investigate the simultaneous adsorption capacity of shell-based biochars for multi-component VOCs, as well as the underlying competitive adsorption mechanisms. In this study, dynamic adsorption experiments were conducted using PP biochar in binary (*i.e.*, toluene–chlorobenzene) and ternary (*i.e.*, benzene–toluene–chlorobenzene) systems. The competitive adsorption behavior was quantitatively analyzed by evaluating the breakthrough curves.

The breakthrough curve for the toluene–chlorobenzene binary system (Fig. 11) differs significantly from that of the single-component chlorobenzene adsorption curve. Notably, the toluene outlet concentration exceeded the inlet concentration during the later stage of adsorption, indicating that pre-adsorbed toluene molecules were desorbed and replaced by chlorobenzene. This phenomenon indicates a competitive adsorption advantage of chlorobenzene over toluene. Additionally, the breakthrough adsorption time of chlorobenzene is significantly longer than that of toluene. This observation supports the preferential adsorption of chlorobenzene in the binary system.

The breakthrough curves for the benzene–toluene–chlorobenzene ternary system (Fig. 12) exhibit more complex competitive interactions. The outlet concentrations of both benzene and toluene exceeded their inlet concentrations, manifesting as "peak overshoot effects". In general, benzene had a higher peak concentration, and its peak appeared earlier than that of toluene. After the desorption of benzene subsided, toluene began to adsorb and ultimately reached its own peak concentration. This phenomenon was attributed to the dominant competitive advantage of chlorobenzene within the ternary mixture. Chlorobenzene preferentially occupied the available adsorption sites through a displacement mechanism, thereby inducing the desorption of pre-adsorbed benzene and toluene. This behavior was attributed to the stronger molecular polarity and other inherent physicochemical properties of chlorobenzene, which enhanced its adsorption affinity and competitive strength over the other two VOCs.

The adsorption capacities of the different VOC components under various adsorption conditions were calculated based on the breakthrough curves (Table 5 and Fig. 13). The results indicated that the adsorption performance of PP biochar for VOCs is significantly influenced by the types and concentrations of components in the system. The adsorption capacity increased in the order, single-component < binary-component < multi-component systems. Notably, the total adsorption capacity in the multi-component system was significantly higher than the sum of the individual single-component adsorption capacities, revealing a multi-component adsorption enhancement effect. Specifically, under single-component

Table 5 Benzene, toluene, and chlorobenzene single and multi-component VOC saturation adsorption capacities of PP biochar

Adsorbate system	Adsorbate	Saturated adsorption capacity (mg g^{-1})
Single-component	Chlorobenzene	572.5
Binary-component	Chlorobenzene	340.7
	Toluene	272.5
Multi-component	Chlorobenzene	313.0
	Toluene	241.7
	Benzene	108.3

 © 2026 The Author(s). Published by the Royal Society of Chemistry

Open Access Article. Published on 12 January 2026. Downloaded on 4/29/2026 2:22:39 PM.
This article is licensed under a Creative Commons Attribution-NonCommercial 3.0 Unported Licence.

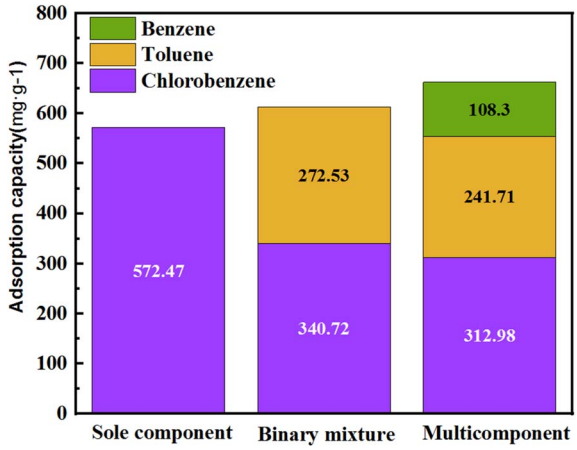

Fig. 13 Single and multi-component VOC saturation adsorption capacities of PP biochar.

conditions, PP biochar exhibited the highest saturation adsorption capacity for chlorobenzene, reaching 572.5 mg g^{-1}. This was higher than its adsorption capacity for toluene, indicating that chlorobenzene has stronger affinity or better matching with the available adsorption sites on the biochar surface.

In the binary system (chlorobenzene–toluene), the saturation adsorption capacities of chlorobenzene and toluene were 340.7 and 272.5 mg g^{-1}, respectively, totaling 613.2 mg g^{-1}. This value is slightly higher than the single-component adsorption capacity of chlorobenzene alone but lower than the theoretical sum of the individual single-component capacities (chlorobenzene + toluene). This result suggested that a certain degree of competitive adsorption emerged in the binary system, although it did not significantly reduce the overall adsorption capacity.

In the more complex multi-component system (chlorobenzene–toluene–benzene), the saturation adsorption capacities of PP biochar for the three VOCs were 313.0 mg g^{-1} for chlorobenzene, 241.7 mg g^{-1} for toluene, and 108.3 mg g^{-1} for benzene, totaling 663.0 mg g^{-1}. This value is significantly higher than both the single-component adsorption capacity for chlorobenzene (572.5 mg g^{-1}) and the total adsorption capacity in the binary system (613.2 mg g^{-1}). Thus, the total adsorption capacity in the multi-component system exceeded the sum of the individual single-component adsorption capacities, representing a synergistic enhancement in multi-component adsorption.

The overall adsorption capacity increased as follows: toluene alone < chlorobenzene alone < chlorobenzene + toluene < chlorobenzene + toluene + benzene. This trend is consistent with the multi-component adsorption enhancement phenomenon reported by Yu *et al.*[36] A study by Shiue *et al.*[37] also concluded that when VOC concentrations increase, adsorbate molecules may form localized aggregates through non-covalent interactions, such as van der Waals forces, π–π stacking, or hydrogen bonding. These interactions facilitate efficient occupation of active sites on the adsorbent surface, thereby enhancing the packing capacity per unit mass of adsorbent.

In this study, the multi-component VOC system contained a mixture of three aromatic compounds: benzene, toluene, and chlorobenzene. Strong π–π interactions exist between their benzene rings and the graphitized regions of the biochar. When these aromatic molecules coexist, they can form an ordered co-adsorption layer on the carbon material surface *via* π–π interactions. This co-adsorption behavior likely modified the properties of the adsorbate–adsorbent interface, leading to more efficient utilization of adsorption sites and, consequently, a slight increase in the adsorption capacity for individual components. Furthermore, chlorobenzene has a certain degree of polarity due to the chlorine atom, potentially enabling dipole–dipole interactions or hydrogen bonding with oxygen-containing functional groups on the biochar surface. Such interactions could anchor some chlorobenzene molecules thereby (i) creating a more favorable adsorption environment for the non-polar benzene and toluene molecules or (ii) altering the structure of the surface adsorption layer in a way that promotes the adsorption of other molecules.

Additionally, the biochar material prepared in this study has an ultra-high specific surface area and unique surface chemistry, providing abundant adsorption sites. This abundance likely reduces the significance of direct competition between molecules, allowing the aforementioned synergistic co-adsorption mechanism to dominate. If the total concentration remains below saturation levels, this synergistic effect can manifest as an overall enhancement. Ultimately, this enables different VOCs to occupy adsorption sites in a complementary manner, leading to a greater total adsorption capacity.

3.3.2 Competitive adsorption mechanism of multi-component VOCs. The competitive adsorption behavior of multi-component VOCs is related to the molecular characteristics of the adsorbates.[34,38,39] The key physicochemical properties influencing the adsorption competition of benzene, toluene, and chlorobenzene include saturated vapor pressure, polarity, and molecular kinetic diameter (Table 6). Adsorbate molecules with lower saturated vapor pressures tend to have stronger interactions with the adsorbent, resulting in higher equilibrium adsorption capacities. Molecules with smaller molecular kinetic diameters and higher polarity are more likely

Table 6 Physical and chemical properties of benzene, toluene, and chlorobenzene

VOC	Molecular formula	Molar mass (g mol^{-1})	Boiling point (°C)	Saturated vapor pressure at 30 °C (kPa)	Polarity
Benzene	C_6H_6	78.11	80.1	15.85	Nonpolar
Toluene	C_7H_8	92.14	110.6	4.9	Nonpolar
Chlorobenzene	C_6H_5Cl	112.56	131.7	2.08	Polar

Open Access Article. Published on 12 January 2026. Downloaded on 4/29/2026 2:22:39 PM.
This article is licensed under a Creative Commons Attribution-NonCommercial 3.0 Unported Licence.

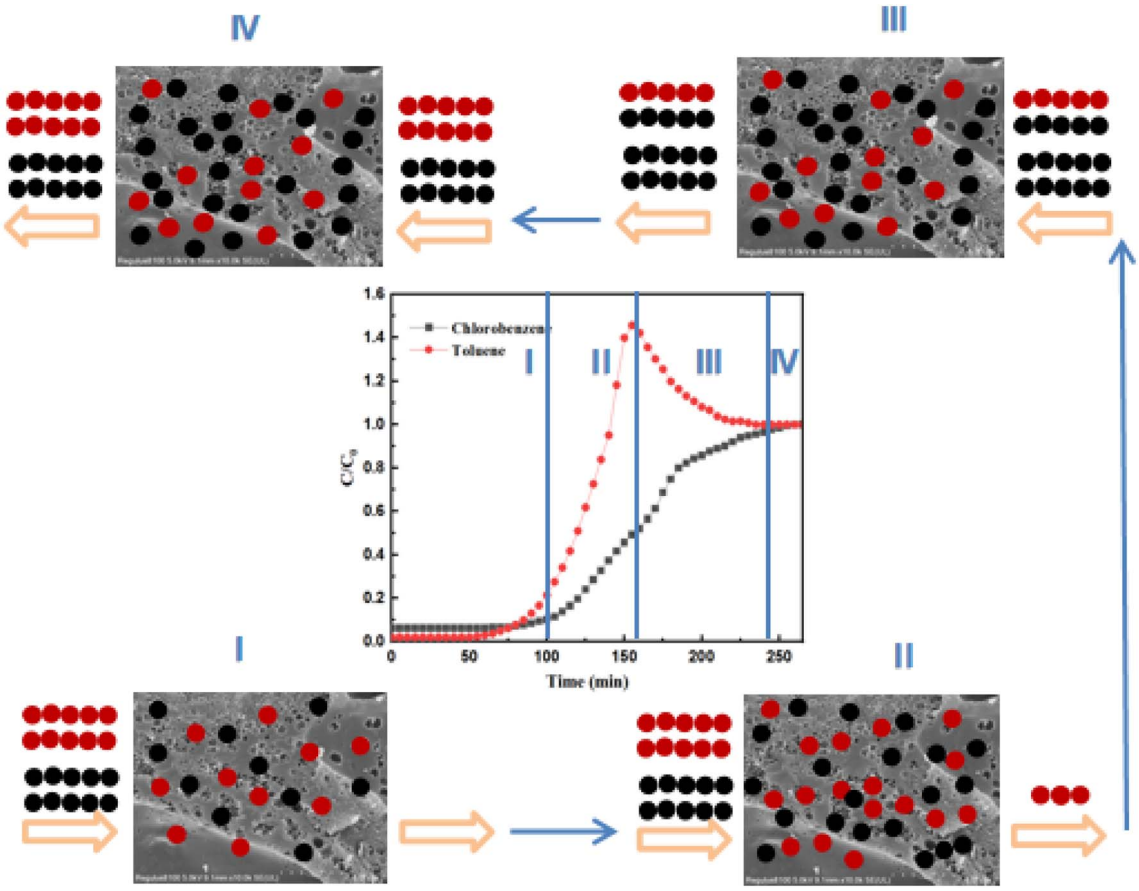

Fig. 14 Competitive adsorption of toluene and chlorobenzene.

to enter micropores and interact with surface functional groups, thereby enhancing their adsorption affinities. Similar phenomena have been validated in previous studies. For example, our research group previously observed a displacement phenomenon in which toluene displaced benzene during the adsorption of binary VOCs on alkali-modified corn cob biochar.[40] Other researchers have demonstrated the competitive substitution behaviors of these VOCs, such as chlorobenzene displacing benzene or toluene.[41,42] However, a systematic understanding of the competitive adsorption process involving three-component VOC mixtures remains limited.

Based on molecular characteristics, chlorobenzene has a lower saturated vapor pressure than toluene and benzene; it also contains a polar C–Cl bond, whereas benzene and toluene are nonpolar molecules. Overall, chlorobenzene has a lower saturated vapor pressure, stronger polar interactions, and better compatibility with micropores and oxygen-containing functional groups on the adsorbent surface. As a result, chlorobenzene dominates the competitive adsorption process in the tested multi-component systems. It sequentially displaces toluene and benzene (*i.e.*, adsorption sequence: chlorobenzene > toluene > benzene), as reflected in the longer saturation adsorption time for chlorobenzene. Furthermore, benzene has a higher desorption peak concentration than toluene, resulting in a significant difference in desorption intensity among the three VOCs.

Additionally, the breakthrough behavior of the multi-component VOCs follows a consistent pattern. Specifically, components with higher saturated vapor pressures preferentially break through, while those with lower saturated vapor pressures are desorbed and replaced. In a multi-component VOC system, components with higher saturated vapor pressures, such as benzene and toluene, tend to break through the adsorbent layer first and reach adsorption saturation earlier. Then, they are desorbed and replaced by components with lower saturated vapor pressures, such as chlorobenzene, through a competitive displacement mechanism. This study showed that benzene and toluene were desorbed in sequence, and toluene and chlorobenzene reached adsorption equilibrium at approximately the same time. When chlorobenzene, which has the lowest saturated vapor pressure, began to elute from the adsorbent, the desorption rate of toluene reached its maximum. This phenomenon is consistent with the features of the breakthrough curves for the three-component VOC system.

The competitive adsorption of toluene and chlorobenzene by PP biochar can be divided into four distinct stages. In stage 1, both toluene and chlorobenzene are fully adsorbed, with toluene being the first to elute from the adsorbent and reach saturation. In stage 2, the adsorbed toluene is desorbed from the adsorbent and gradually replaced by chlorobenzene. In stage 3, this continues until chlorobenzene begins to elute from the adsorbent, after which, toluene continues to desorb until

 © 2026 The Author(s). Published by the Royal Society of Chemistry

Open Access Article. Published on 12 January 2026. Downloaded on 4/29/2026 2:22:39 PM.
This article is licensed under a Creative Commons Attribution-NonCommercial 3.0 Unported Licence.

both toluene and chlorobenzene simultaneously reach equilibrium. Finally, in stage 4, toluene and chlorobenzene reach and maintain a state of equilibrium. Similar stages of competitive adsorption between benzene and chlorobenzene have been reported.[36,43] In three-component adsorption (benzene–toluene–chlorobenzene), benzene first reaches adsorption–desorption equilibrium, and toluene and chlorobenzene reach equilibrium later and simultaneously (Fig. 14).

4 Conclusions

This report describes the preparation of hierarchical porous biochar materials with high SSA derived from shell-based agricultural waste biomass employing a green modification strategy involving sodium phytate and sodium hydroxide. The physicochemical properties of the materials were systematically investigated, and their adsorption performance and competitive adsorption mechanisms for chlorinated VOCs were analyzed. The PP biochar had an exceptionally high saturation adsorption capacity of 572.5 mg g^{-1} for chlorobenzene, reflecting its well-developed microporous structure, favorable pore size distribution, abundant surface oxygen-containing functional groups, and amorphous-graphitized microcrystalline structure. In competitive adsorption systems involving multi-component chlorinated VOCs, chlorobenzene demonstrated a significant competitive adsorption advantage, thus confirming the strong adaptability and selective adsorption capability of PP biochar in complex VOC environments. The green biochar modification approach proposed herein overcomes the limitations of traditional chemical activation methods, such as pollution and equipment corrosion, to enable agricultural waste valorization. The prepared PP biochar can be prepared at low cost in an environmentally friendly process and exhibits excellent adsorption performance for chlorobenzene, demonstrating broad application prospects in the treatment of industrial exhaust gases containing chlorinated VOCs. The results discussed herein also provides insights and technical pathways for the development of efficient and environmentally friendly VOC adsorption materials.

Author contributions

Dan He: writing – original draft, software, methodology, investigation, writing – review & editing, writing – review & editing. Jiao Wang: software, investigation; writing – review & editing. Wei Deng: software, investigation; writing – review & editing. Xiang Tu: software, investigation, supervision, project administration, funding acquisition. Chenglong Yu: conceptualization, validation, supervision, investigation, software, writing – original draft, writing – review & editing, project administration, funding acquisition. Jiangbo Xiong: software, investigation, methodology. Meijuan Lu: software, investigation.

Conflicts of interest

The authors declare that they have no known competing financial interests or personal relationships that could have appeared to influence the work reported in this paper.

Data availability

All data generated or analyzed during this study are included in this published article and its supplementary information (SI) files. Supplementary information is available. See DOI: https://doi.org/10.1039/d5ra07060k.

Acknowledgements

This research was financially supported by the National Natural Science Foundation of China (Grant No. 52160009; 22466020), Key R&D Program of Jiangxi Province, China (Grant No. 20243BBH81036), the Natural Science Foundation of Jiangxi Province (Grant No. 20242BAB23053), and the Training Program for Academic and Technical Leaders of Major Disciplines in Jiangxi Province, China (Grant No. 20212BCJL23054). We also would like to thank Suzhou Deyo Bot Advanced Material Co., Ltd for providing support on material characterization.

References

1 H. F. Yang, G. N. Liang, X. Y. Sun and S. M. Wu, *Carbon Lett.*, 2024, **34**, 1851–1875.
2 T. Lu, C. Zhang, F. Du, C. Zhang, R. Zhang, P. Liu and J. Li, *J. Colloid Interface Sci.*, 2023, **641**, 791–802.
3 X. Yao, K. Wan, W. Yu and Z. Liu, *Front. Environ. Sci. Eng.*, 2024, **18**, 110.
4 M. Ren, J. Wang, Z. Wang, S. Sun, J. Qiu, Y. Shi, Z. Wang and Y. Xie, *J. Environ. Chem. Eng.*, 2022, **10**, 107319.
5 J. Liao, K. Yin, X. D. Chen and B. C. Huang, *New J. Chem.*, 2024, **48**, 10273–10283.
6 L. Zhu, D. Shen and K. H. Luo, *J. Hazard. Mater.*, 2020, **389**, 122102.
7 Y. Chen, H. Xu and M. Shahnawaz, *Crit. Rev. Environ. Sci. Technol.*, 2025, **55**, 1097–1123.
8 S. H. Boroojerdi, M. M. Mohammadi and F. Bahadoran, *RSC Adv.*, 2025, **15**, 27311.
9 R. Wei, Z. Cheng, J. Chen, J. Liu, J. Wang, D. Chen and Z. Lu, *J. Environ. Sci.*, 2026, **162**, 1–13.
10 Z. Zhao, W. Wu, W. Li, B. Li, Z. Shui, X. Wang, G. Jiang, G. Li, J. Cheng, Z. Zhang and Z. Hao, *Sep. Purif. Technol.*, 2025, **354**, 129271.
11 T. Y. Cheng, J. J. Li, X. W. Ma, L. Zhou, H. Wu and L. J. Yang, *Environ. Pollut.*, 2022, **295**, 118714.
12 W. C. Ji, M. P. Zhang, X. J. Fan, H. M. Zou, Y. Y. Meng, Y. B. Cai, F. D. Meng, H. Y. Wang and Y. Lou, *Langmuir*, 2023, **39**, 11016–11027.
13 F. Sadegh, N. Sadegh, W. Wongniramaikul, R. Apiratikul and A. Choodum, *Process Saf. Environ. Prot.*, 2024, **182**, 559–578.
14 Y. J. Wang, D. Yuan, S. G. Wan, S. Q. Yi, J. L. Wu and L. Sun, *J. Environ. Chem. Eng.*, 2025, **13**, 115669.
15 C. Yang, G. Miao, Y. Pi, Q. Xia, J. Wu, Z. Li and J. Xiao, *Chem. Eng. J.*, 2019, **370**, 1128–1153.
16 J. J. Zhang, J. G. Shao, X. Zhang, H. Jiang, S. B. Zhang, S. H. Zhang, H. P. Yang and H. P. Chen, *Fuel*, 2024, **372**, 132127.

Open Access Article. Published on 12 January 2026. Downloaded on 4/29/2026 2:22:39 PM.
This article is licensed under a Creative Commons Attribution-NonCommercial 3.0 Unported Licence.

17 J. Wen, Z. Liu, H. Xi and B. Huang, *J. Environ. Sci.*, 2023, **126**, 123–137.
18 L. Matejová, M. Vastyl, Z. Jankovská, P. Cichonová, P. Peikertová, I. Sedenková, G. Cruz, J. Veliz and O. Kania, *J. Anal. Appl. Pyrolysis*, 2024, **181**, 106630.
19 Ö. Şahin, C. Saka, A. A. Ceyhan and O. Baytar, *Sep. Sci. Technol.*, 2015, **50**, 886–891.
20 Y. Sheng, Q. Ren and Q. Q. Dong, *Sustainability*, 2023, **15**, 14803.
21 T. Y. Cheng, J. J. Li, X. W. Ma, L. J. Yang, L. Zhou and H. Wu, *Environ. Sci. Pollut. Res.*, 2023, **30**, 91262–91275.
22 X. D. Chen, J. Liao, K. Yin, L. Cheng, Z. W. Yang, Z. W. Liu and B. C. Huang, *J. Environ. Chem. Eng.*, 2025, **13**, 115168.
23 S. Zhu, H. Xu, M. S. Khan, M. Xia, F. Wang and Y. Chen, *Water Res.*, 2025, **272**, 122997.
24 D. Di, J. Xiao and B. Zhao, *Carbon Res.*, 2025, **4**, 35.
25 C. Yu, J. Dan and Z. Liu, *Fuel*, 2024, **358**, 130136.
26 D. Z. Sun, F. Y. Li, J. W. Jin, S. Khan, K. M. Eltohamy, M. M. He and X. Q. Liang, *Sci. Total Environ.*, 2022, **829**, 154599.
27 M. W. U. Zaman, A. D. Phule, T. G. Senthamaraikannan, S. Y. Kim, S. Elkaee, J. H. Yang and D. Lim, *Environ. Res.*, 2025, **269**, 26.
28 Q. Xu, Y. Jin, F. Zheng and J. Lu, *Sep. Purif. Technol.*, 2023, **324**, 124595.
29 M. Kuddushi, X. Deng, J. Nayak, S. Zhu, B. B. Xu and X. Zhang, *ACS Appl. Bio Mater.*, 2023, **6**, 3810–3822.
30 Y. Yang, B. Lin, C. Sun, M. Tang, S. Lu, Q. Huang and J. Yan, *Sci. Total Environ.*, 2021, **773**, 145453.
31 H. Cheng, Y. Sun, X. Wang, S. Zou, G. Ye, H. Huang and D. Ye, *J. Hazard. Mater.*, 2020, **392**, 122298.
32 M. Wahad Uz Zaman, A. Dattatray Phule, S. Elkaee, S. Yi Kim and J. Hwan Yang, *Sep. Purif. Technol.*, 2025, **353**, 128378.
33 S. Bagheri Novair, M. Cheraghi, F. Faramarzi, B. Asgari Lajayer, V. Senapathi, T. Astatkie and G. W. Price, *Ecotoxicol. Environ. Saf.*, 2023, **263**, 115228.
34 M. S. Ece and S. Kutluay, *J. Environ. Chem. Eng.*, 2022, **10**, 107389.
35 D. Li, X. Guo, L. Wang, H. Deng, Z. Zhang, J. Ma and H. He, *Microporous Mesoporous Mater.*, 2025, **381**, 113365.
36 H. Yu, F. Lin, K. Li, W. Wang, B. Yan, Y. Song and G. Chen, *Environ. Res.*, 2021, **202**, 111687.
37 A. Shiue, Y. Kang, S. Hu, G. Jou, C. Lin, M. Hu and S. Lin, *Build. Sci.*, 2010, **45**, 2123–2131.
38 E. Batur and S. Kutluay, *J. Environ. Chem. Eng.*, 2022, **10**, 107565.
39 H. Rajabi, M. Hadi Mosleh, T. Prakoso, N. Ghaemi, P. Mandal, A. Lea-Langton and M. Sedighi, *Chemosphere*, 2021, **283**, 131288.
40 D. He, J. Wu, C. Yu, B. Huang, X. Tu, D. Li, X. Jia, J. Dan, Z. Fang, Z. Dai, R. Liu and Q. Zhou, *J. Chem. Technol. Biotechnol.*, 2023, **98**, 2051–2064.
41 C. Long, Q. Li, Y. Li, Y. Liu, A. Li and Q. Zhang, *Chem. Eng. J.*, 2010, **160**, 723–728.
42 X. Zhao, X. Zeng, Y. Qin, X. Li, T. Zhu and X. Tang, *Chemosphere*, 2018, **206**, 285–292.
43 X. Huang, M. Tang, H. Li, L. Wang and S. Lu, *Chemosphere*, 2023, **313**, 137513.

 © 2026 The Author(s). Published by the Royal Society of Chemistry